Fracture network localization preceding catastrophic failure in triaxial compression experiments on rocks

Jessica McBeck[1], Yehuda Ben-Zion[2], François Renard[1,3]

[1]The Njord Centre, Departments of Geosciences and Physics, University of Oslo, Oslo, Norway.

[2]Department of Earth Sciences and Southern California Earthquake Center, University of Southern California, Los Angeles, CA, USA.

[3]University Grenoble Alpes, University Savoie Mont Blanc, CNRS, IRD, ISTerre, Grenoble, France

*** Correspondence:**
Jessica McBeck
j.a.mcbeck@geo.uio.no

Key words: fractures$_1$, localization$_2$, X-ray tomography$_3$, crystalline rock$_4$, triaxial compression$_5$

Abstract

We quantify the spatial distribution of fracture networks throughout six in situ X-ray tomography triaxial compression experiments on crystalline rocks at confining stresses of 5-35 MPa. Tracking the proportion of the cumulative volume of fractures with volumes >90th percentile to the total fracture volume, $\sum v_{90}/v_{tot}$ indicates that the fracture networks tend to increase in localization toward these largest fractures for up to 80% of the applied differential stress. The evolution of this metric also matches the evolution of the Gini coefficient, which measures the deviation of a population from uniformity. These results are consistent with observations of localizing low magnitude seismicity before large earthquakes in southern California. However, the proportion of the maximum fracture volume to the total fracture volume does not increase monotonically. Experiments with higher confining stress tend to experience greater localization. To further quantify localization, we compare the geometry of the largest fractures, with volumes >90th percentile, to the best fit plane through these fractures immediately preceding failure. The r^2 scores and the mean distance of the fractures to the plane indicate greater localization in monzonite than in granite. The smaller mean mineral diameter and lower confining stress in the granite experiments may contribute to this result. Tracking these various metrics of localization reveals a close association between macroscopic yielding and the acceleration of fracture network localization. Near yielding, $\sum v_{90}/v_{tot}$ and the Gini coefficient increase while the mean distance to the final failure plane decreases. Macroscopic yielding thus occurs when the rate of fracture network localization increases.

Manuscript length: 8900 words, 12 figures, 1 table

1 Introduction

Preexisting weaknesses control how and when rocks fail because they concentrate shear and tensile stresses that promote fracture propagation under relatively low differential stress (e.g., *Griffith*, 1921). These early fractures tend to propagate parallel to the maximum compression direction, σ_1, and open perpendicular to σ_3 in rocks (e.g., *Peng & Johnson*, 1972; *Moore & Lockner*, 1995; *Wu et al*., 2000; *Miao et al.*, 2021). Following the wing crack model of fracture network development (e.g., *Brace et al*., 1966; *Horii & Nemat-Nasser*, 1986; *Sammis & Ashby*, 1986; *Kemeny & Cook*, 1987), the initial propagation of a fracture from an inclined preexisting fracture is stable, so increasing stress must drive further propagation. Laboratory observations suggest that when the length of a fracture is comparable to the interfracture spacing, fractures begin to interact with each other, prompting linkage and coalescence (e.g., *Wong*, 1982; *Kranz*, 1983; *Rawling et al*., 2002). This transition from distributed, isolated fractures to coalescing, interacting, and localizing arrays of fractures is associated with a transition from stable to unstable propagation (e.g., **Figure** 1). The spatial distribution of the evolving fracture network thus may provide key information about the proximity of the system to failure. Indeed, fracture network clustering is a key predictor of the timing of catastrophic failure in triaxial compression experiments (*McBeck et al*., 2020a). Similarly, increasing localization and clustering of low magnitude seismicity preceded several $M > 7$ earthquakes in southern and Baja California (*Ben-Zion and Zaliapin*, 2020).

Field observations and laboratory experiments show how deformation can become more localized toward macroscopic failure in the laboratory, and with increasing total slip and slip-rate along faults in the field (e.g., *Segall & Pollard*, 1983; *Chen & Spetzler,* 1993; *Bergbauer & Martel*, 1999; *Pachell & Evans*, 2002; *Ben-Zion & Sammis*, 2003; *Schubnel et al*., 2003; *Kattenhorn & Marshall*, 2006; *Joussineau et al*., 2007; *Moir et al*., 2010; *Zhao et al.*, 2018; *Kandula et al*., 2019; *Renard et al*., 2019a, b; *McBeck et al*., 2020a, b). Locations of acoustic emissions (AEs) captured during rock deformation experiments under triaxial compression loading suggest that the AEs localize from a diffuse cloud to a narrower zone with increasing deformation (*Locker et al*., 1991; *Aben et al*., 2019). Some experiments show that AEs can propagate across the rock sample, from a smaller cluster of AEs at one edge of the rock sample to a system-spanning, elongate cluster (*Benson et al*., 2007). Some clusters of AEs may include a process zone and subsequent damage zone (*Lei et al*., 2000). Tensile fracturing and low *b* values with a few large events characterize deformation in the process zone, while shear fracturing and higher *b* values with a greater number of larger events characterize deformation in the damage zone. These laboratory observations suggest that fracture linkage is the dominant form of fracture network development following macroscopic fault formation. Additional analyses identify a link between *b* values and the spatial distribution of AEs in experiments on precut granite cores that contain faults with varying degrees of roughness (*Goebel et al*., 2017). Rougher faults have more distributed AEs and higher *b* values than smoother faults, which produce more localized deformation with larger rupture areas and thus lower *b* values.

In situ X-ray tomography experiments that capture images of three-dimensional fracture networks at different times provide additional evidence of deformation localization preceding catastrophic failure. Observations from X-ray tomography experiments indicate that fracture networks can evolve from isolated fractures that trend parallel to σ_1, to a linked array of fractures that trends oblique to σ_1 (*Zabler et al*., 2008; *Kandula et al*., 2019; *Renard et al*., 2018, 2019a). Similar experiments on granite and other low porosity crystalline rocks show a similar tendency of increasing localization toward failure: from initially distributed fractures to a system-spanning fault network (*Renard et al.*, 2017, 2019b). However, some experiments on these rock types do not reveal such system-spanning faults preceding macroscopic failure

(*Renard et al*., 2019a, b; *McBeck et al*., 2021). In these experiments, the fracture networks remain relatively distributed with several large fractures, rather than one dominant system-spanning fault.

These previous analyses did not systematically compare the varying expressions of fracture network localization, and did not examine why different experiments, under varying confining stresses and on different rock types, experienced varying expressions of localization. Here, we quantify and compare the evolving spatial distribution of fracture networks throughout six in situ X-ray tomography triaxial compression experiments on low porosity crystalline rocks: granite and monzonite. We assess the idea that one dominant fracture continually grows at the expense of others by tracking the proportion of the volume of the maximum fracture, v_{max}, to the total fracture volume, v_{tot}, throughout each experiment. We also examine if the set of the largest fractures continually dominates deformation by tracking the sum of the volume of the fractures with volumes >90th percentile, relative to the total fracture volume, $\sum v_{90}/v_{tot}$, and the Gini coefficient, which measures the deviation of a population from a uniform distribution (*Gini*, 1921). To further quantify the localization of the fracture networks, we compare the geometry of the set of the largest fractures to a plane. We find the best fit plane through the fractures with volumes >90th percentile in the tomogram immediately preceding failure, and then calculate the distance between these fractures and the plane, and the r^2 score of the fractures and the plane. Tracking these various metrics of localization reveals fundamental insights into the temporal evolution of localization toward failure, including intermittent phases of delocalization, the influence of confining stress and rock type on localization, and the temporal correlation between macroscopic yielding and fracture network localization.

2 Methods

2.1 In situ X-ray tomography

We use the X-ray transparent triaxial deformation apparatus Hades (*Renard et al*., 2016) installed at beamline ID19 at the European Synchrotron and Radiation facility to deform the rock cores. This apparatus enables acquiring X-ray tomograms of the rock core while it is inside the apparatus at the applied differential stress conditions. In these experiments, we apply a constant confining stress between 5 and 35 MPa (**Table** 1) using oil surrounding the jacket that contains the rock core, and then increase the axial stress in steps of 0.5-5 MPa, with smaller increases of axial stress closer to macroscopic failure (**Figure** 2), at ambient temperature conditions. After each stress step, we acquire 1600 radiographs at 32 bytes gray scale resolution of X-ray absorption while the sample is rotated over 180° within 1.5 minutes. The final reconstructed tomogram contains 1600 x 1600 x 1600 voxels with 6.5 µm/voxel spatial sampling. Due to the stress-controlled loading conditions, the rocks fail in a sudden stress drop. The final scan is acquired typically within 0.5 MPa of the final failure stress. We measure the axial contraction of the rock sample using the tomograms because the shortening of the rock core is visible in the three-dimensional images.

The rock samples are cylinders 1 cm tall and 4 mm wide. We perform three experiments on Westerly granite and three experiments on monzonite. Granite and monzonite are both low porosity crystalline rocks dominated by quartz and feldspar. The main difference between these rocks is that the mean grain size of the granite is 100-200 micrometers, while monzonite has a mean grain size of 300-400 micrometers (e.g., *Aben et al*., 2016). Each rock

sample was deformed without fluid, except for monzonite #4, which included 5 MPa of deionized water as pore fluid pressure.

Each experiment includes the typical three stages of rock deformation in the brittle regime: 1) an early linear phase, 2) yielding, and 3) macroscopic failure (**Figure** 2). Due to the approximately linear relationship between the axial contraction and differential stress early in each experiment, we may fit a line through the data to identify the yield point. We identify the yield point when the data begins to diverge from the linear fit by more than 5%. Later, we compare the microscopic observations of fracture network development to the timing of the macroscopic yielding. The images of the X-ray tomograms of each experiment are publicly available (*Renard*, 2017, 2018, 2021).

2.2 Segmentation of fracture networks

During the reconstruction of the radiographs to three-dimensional volumes, we applied corrections to remove acquisition noise, including ring artefacts, and to smooth variations in the intensity of the X-ray source during the experiment. To remove noise from the reconstructed images, we preprocessed these data using the commercial image analysis software AvizoFire™, including denoising the volumes using a non-local-means filter (*Buades et al.,* 2005).

The reconstructed tomograms are three-dimensional representations of the local density of the material. Pores and fractures may be distinguished from the solid rock because they have distinct ranges of densities. We segment the rock into solid and fractures using a standard global thresholding technique. We identify the local minimum in the histogram of the gray scale values of the tomogram, indicative of density, that separates the solid material from the fractures and pores (**Figure** S1). We identify this minimum threshold by fitting two Gaussian distributions to the two portions of the histogram that correspond to the solid material and fractures. We identify the threshold between the phases at the gray scale value when the second derivative of this cumulative Gaussian distribution is closest to zero. A second derivative equal to zero indicates an inflection point between the two Gaussian distributions, which we use as the threshold to separate the solid from the voids.

2.3 Gini coefficient

We use several metrics to quantify localization, including the Gini coefficient. The Gini coefficient uses the Lorenz curve of a distribution to measure the deviation from a uniform distribution (e.g., *Gini*, 1921; *Ben-Zion & Zaliapin*, 2020). The Lorenz curve shows the proportion of the total amount of a population, such as fracture volume, that is included in the bottom percentile of a population. The Gini coefficient is one minus twice the integral of the Lorenz curve (**Figure** S2). Thus, larger Gini coefficients indicate that the total volume of the fractures in a network is dominated by a few fractures, whereas lower Gini coefficients indicate that the total volume is more equally distributed among all the fractures.

3 Results

3.1 Localization toward the largest fractures

To gain a general understanding of fracture network localization in these experiments, we first examine the fracture networks in the final five scans before system-size failure in two

experiments (**Figure** 3). These two experiments share some fundamental similarities in fracture network development preceding macroscopic failure. In the final stages of the monzonite #5 experiment (**Figure** 3a), the largest fractures appear first relatively randomly spread throughout the rock core. With increasing differential stress, the fractures grow in volume and link with each other. In the scan immediately preceding failure, the fracture network extends from the top to the bottom of the core. Similar to the monzonite #5 experiment, initially the fracture and pore network in the granite #2 experiment is relatively diffusely distributed (**Figure** 3b). Then, with increasing differential stress, several fractures propagate and coalesce to form elongated system-spanning fault networks.

The fracture networks in these experiments also suggest differences in the localization process between rock types. In the monzonite #5 experiment, the identified fracture network extends from the top to the bottom of the core, and also has a wide lateral extent, perpendicular to σ_1. In the granite #2 experiment, the largest fractures extend from the top to the bottom of the core, but are more narrowly constrained in the lateral direction. Thus, the fracture network appears more localized in the granite #2 experiment immediately preceding failure than the monzonite #5 experiment. Next, we assess the validity of these observations by quantifying the localization of the fracture networks.

To quantify the coalescence of the fracture networks throughout triaxial compression, we first track the proportion of the maximum fracture volume to the total volume of all the fractures, v_{max}/v_{tot}, in each scan acquired throughout the experiments (**Figure** 4). High v_{max}/v_{tot} indicates that the largest, most volumetric, fracture in the network dominates the network. Increasing v_{max}/v_{tot} indicates that the largest fracture continually dominates an increasing proportion of the fracture network. Following the idea that the fracture networks coalesce into one dominant fracture, v_{max}/v_{tot} should continually increase with differential stress. However, only two of the experiments (monzonite #3 and granite #4) show generally increasing v_{max}/v_{tot}, with a few episodic decreases. Instead, the majority of the experiments experience delocalization away from the largest fracture, with prolonged phases of decreasing v_{max}/v_{tot}. The granite #1 and #2 experiments host relatively constant v_{max}/v_{tot} until near macroscopic failure, and then sharp drops in v_{max}/v_{tot}. The monzonite #4 experiment also hosts a sharp drop in v_{max}/v_{tot} near failure. These sharp drops indicate that many smaller fractures are propagating and lengthening in the final stages preceding failure, while the largest fracture is growing at a slower rate relative to the cumulative influence of all of the smaller fractures.

The experiments that do not host a sharp drop in v_{max}/v_{tot} near failure show either sharp (monzonite #5) or more gradual (monzonite #3, granite #4) increases in v_{max}/v_{tot} following yielding and preceding macroscopic failure. Thus, following yielding, the final fracture network that develops in half of the experiments is dominated by the largest fracture that grows at the expense of the other fractures, and likely coalesces with several of the preexisting large fractures. In the other set of the experiments, the final fracture network is dominated by several large fractures, and not only one.

The metric of localization, v_{max}/v_{tot}, reveals that fracture network development does not always follow the idealized evolution of one fracture continually growing at the expense of others. Rather, the rocks experience phases of delocalization away from the largest fracture, as well as the localization of deformation toward it. Due to this contrasting behavior, we next examine the localization of the few largest fractures, rather than only the absolute maximum. We track the set of fractures with volumes >90th percentile of the fracture volumes in each tomogram (i.e., the cumulative volume of the top 10th percentile fractures at each stress step).

We then examine the evolution of the proportion of the sum of their fracture volumes, $\sum v_{90}$, to the total fracture volume, v_{tot}, with increasing differential stress. Increasing $\sum v_{90}/v_{tot}$ indicates increasing localization toward the largest set of fractures in the network, with volumes >90th percentile. We also test the influence of changing this threshold, and do not observe significant differences in the results.

In all but one of the experiments (granite #1), the largest fractures host generally increasing proportions of the total fracture network throughout loading (**Figure** 5). The granite #1 experiment experiences only small changes in $\sum v_{90}/v_{tot}$ (**Figure** 5d, g). Several of the experiments host accelerations in $\sum v_{90}/v_{tot}$ near macroscopic failure (e.g., monzonite #5, granite #4, granite #2). Other experiments show more continuous increases toward failure, without significant changes in the rate of $\sum v_{90}/v_{tot}$ accumulation relative to differential stress (monzonite #3 and #4). The timing of macroscopic yielding and the observed acceleration in $\sum v_{90}/v_{tot}$ are similar in the majority of the experiments (granite #2 and #4, monzonite #4 and #5), but appear to lack a strong correlation in other experiments (e.g., monzonite #3). To test the influence of using different thresholds, we performed this analysis using the 25th, 50th, and 75th percentile thresholds (**Figure** S3). This analysis shows that the overall trends of $\sum v_x/v_{tot}$ when x is 25, 50 and 75 is similar to when x is 90. Although the precise magnitude of $\sum v_x/v_{tot}$ decreases with increasing x, the overall trends remain unchanged. In addition, the evolution of the Gini coefficient matches the evolution of $\sum v_{90}/v_{tot}$ for each experiment (**Figure** S4).

In summary, the majority of the experiments experience increasing localization of fracture development toward the largest fractures (**Figures** 5, S3, S4), and the majority of the experiments experience some phases of delocalization away from the one largest fracture (**Figure** 4). Thus, the fracture network that grows at the expense of the other fractures is generally comprised of several fractures, rather than only the largest fracture. Counting the number of the largest fractures throughout each experiment indicates that these fracture networks, composed of fractures with volumes >90th percentile, host hundreds of fractures between the yielding point and macroscopic failure (**Figure** S5).

To more directly compare the signals of localization with the three metrics of the Gini coefficient, $\sum v_{90}/v_{tot}$, and v_{max}/v_{tot}, we now examine the differences of these metrics calculated in the final and initial tomogram of each experiment (**Figure** 6). Comparing the difference in v_{max}/v_{tot} indicates that four of the six experiments experience increasing localization toward the largest fracture from the final to initial scan. Thus, the proportion of the total fracture network contained by the largest fracture increases from the initial to the final scan in four of the six experiments. All but one of the experiments (granite #1) experience localization toward the largest set of fractures, as measured with $\sum v_{90}/v_{tot}$, and the Gini coefficient. The outlier experiment granite #1 produces only a small decrease in $\sum v_{90}/v_{tot}$ from the final to initial scan. Thus, the largest set of fractures, with volumes >90th percentile, comprises a larger proportion of the total fracture network immediately preceding failure than earlier in loading.

The monzonite #5 and granite #4 experiments produce the largest increases in v_{max}/v_{tot}, whereas monzonite #3 and #4 produce the largest increases in $\sum v_{90}/v_{tot}$ and the Gini coefficient. These experiments have higher applied confining stress than the other experiments (granite #1, #2). Thus, higher confining stresses lead to larger increases in localization.

The granite #1 experiment experiences the smallest absolute changes in the localization metrics. The lower applied confining stress and associated shorter yielding phase of the granite #1 experiment (**Figure** 2) may produce the relatively constant localization. Although granite #1 and granite #2 both experience 5 MPa confining stress, granite #1 accumulates less axial strain between yielding and macroscopic failure than granite #2 (**Figure** 2). This shorter yielding phase suggests that the fracture networks grew relatively slowly during yielding in granite #1, producing smaller changes in the axial strain, and smaller changes in the fracture network localization compared to granite #2.

To gain further insight into the different expressions of localization in each experiment, we calculate the proportion of the accumulated differential stress (i.e., time) of the experiment in which the three metrics of localization show increasing localization (**Figure** 7). The differential stress that the system experiences is a proxy for time because we increase the differential stress in steps toward failure, and acquire an X-ray tomogram of the system after each increase in differential stress. Increases in the Gini coefficient, $\sum v_{90}/v_{tot}$, and v_{max}/v_{tot} indicate that the fracture network increases in localization. Thus, we calculate the proportion of the applied differential stress in which each of these three metrics increase from the previous scan (and thus differential stress state). For each metric, we apply a median filter with a bin size of five in order to limit the influence of small perturbations, calculate the slope of the median filtered data, count the number of instances of positive slope, and then sum the differential stress experienced by each scan for all of the scans with a positive slope.

Comparing the percentage of the differential stress in which each of these metrics are localizing indicates that the Gini coefficient or $\sum v_{90}/v_{tot}$ produce higher percentages than v_{max}/v_{tot} in all but one of the experiments (granite #1) (**Figure** 7). Thus, the largest fractures in the network are localizing for longer periods of time than the absolute largest fracture in all but one experiment. Granite #1 is the only experiment in which the largest fracture dominates fracture network localization, rather than the set of the top 10th percentile of the fractures. This experiment increases in localization for about 80% of the time, whereas the Gini coefficient and $\sum v_{90}/v_{tot}$ increase in localization for <40% of the time.

Using the metric that produces the largest percentages of the experimental time (typically the Gini coefficient or $\sum v_{90}/v_{tot}$, none of the experiments experience localization for more than 80% of the time (**Figure** 7). Two of the experiments (monzonite #5, granite #2) experience localization for shorter time intervals, for only about 50% and 5%. Both of these experiments host extended periods of generally decreasing localization early in the experiments, and then brief periods of localization immediately preceding failure (e.g., **Figure** 5). In contrast, the other experiments that host significant degrees of increasing localization, in terms of magnitude and time (monzonite #3, monzonite #4, granite #4), show more prolonged phases of increasing localization that begin before the macroscopic yield point (**Figure** 5).

3.2 Localization toward the final failure plane

The analyses in the previous section indicate that the largest fractures in the network, with volumes >90th percentile, tend to localize for up to 80% of the experimental time (**Figure** 7). To examine the evolving spatial distribution of these largest fractures toward failure, we compare them to the plane that represents the final fracture network immediately preceding failure (e.g., **Figure** 8). We fit this plane to the fractures with volumes >90th percentile in the final scan acquired preceding macroscopic failure using least squares regression in two-dimensions. We fit the plane to the largest set of fractures, rather than only the largest

fracture, because the fracture networks generally localize toward the largest set of fractures (**Figure** 5), rather than the largest fracture (**Figure** 4). To assess how the fracture networks coalesce toward their final geometry, we examine the r^2 score of this final failure plane and the largest set of fractures throughout each experiment (**Figure** 9), and the mean distance between these fractures and the failure plane (**Figures** 10, 11, S6). We calculate the mean distance by finding the closest distance between each large fracture and the failure plane, and then finding the mean of the distances in a given scan.

The fit between the final failure plane and the largest fractures (r^2 score) generally increases toward failure (**Figure** 9). This trend is expected because we calculate the final failure plane using the largest fractures identified in the final scan. However, the fit does not increase monotonically, and instead shows some phases of delocalization away from the plane. The granite #4 experiment hosts the most significant of these drops, in terms of the difference relative to the maximum achieved r^2 score (**Figure** 9f). The monzonite #3 experiment also shows a phase of delocalization, and then stagnating r^2 scores following the macroscopic yield point. Monzonite #3 is also the experiment with the fracture network that most closely fits a plane in the final scan, producing the highest r^2 score (**Figure** 9g).

The granite experiments all show sharp increases in the r^2 score in the final few scans preceding failure. These increases coincide in time with the macroscopic yield point. In contrast, the monzonite experiments show more continuous increases over longer intervals of differential stress. Two of the monzonite experiments reveal changes in the r^2 score near the yield point: decreasing in monzonite #3 and slowing in monzonite #4. The general trends observed in the r^2 score match the trends in the mean distance between each fracture and the plane (**Figure** S6, **Figure** 11).

To further examine the evolving spatial distribution of the largest fractures relative to the final failure plane, we compare the r^2 score and mean distance between the fractures and the plane in the initial and final scans acquired in each experiment (**Figure** 10). The monzonite experiments experience larger r^2 scores in the final scan, and larger increases in the r^2 score than the granite experiments. Thus, the top 10^{th} percentile largest fractures in the final scan more closely match the geometry of a plane in the monzonite experiments than those in the granite experiments. In addition, at the onset of loading, the largest fractures in the monzonite experiments deviate more significantly from a plane than those in the granite experiments. The higher confining stress applied to the monzonite experiments may contribute to the greater localization of the largest fractures toward a plane in this suite of experiments.

Consistent with the trend in the r^2 scores, the monzonite experiments also host lower mean distances between the largest fractures and the failure plane in the final scan compared to the granite experiments (**Figure** 10c). The final mean distance is relatively consistent, near 200 voxels, for the granite experiments. Thus, the largest fractures are more tightly clustered around the final failure plane in the monzonite experiments than the granite experiments. The monzonite experiments also tend to host the largest changes in the mean distance. However, granite #2 also produces a significant change, while monzonite #3 produces a smaller change. These changes occur at least in part because the mean distance in the initial scan is larger (monzonite #3) and smaller (granite #2) than the other experiments.

The mean distance to the final failure plane and the Gini coefficient may correlate with each other. If the largest fractures coalesce from a diffuse to localized distribution, the mean distance should decrease while the Gini coefficient increases. This inverse relationship

generally applies to these experiments (**Figure** 11). Following yielding, the Gini coefficient increases while the mean distance decreases toward failure, in all but the granite #1 experiment (**Figure** 11d). Thus, the fracture networks coalesce from many small distributed fractures to larger well-connected fractures that increasingly localize toward the largest set of fractures, and their approximate failure plane.

4 Discussion

4.1 Fracture network domination

Fracture networks develop through the linkage and coalescence of fractures. In an idealized system without significant mechanical heterogeneities or interaction between neighboring fractures, the localization process should be monotonic (e.g., *Lyakhovsky et al.*, 2011). The relationship between the fracture length and stress intensity factor (e.g., *Isida*, 1971) suggests that the largest fracture in a network should grow at the expense of the others (e.g., **Figure** 12a). If fracture networks under triaxial compression follow this evolution, then the proportion of the maximum fracture volume of the total fracture volume, v_{max}/v_{tot}, should increase continuously toward macroscopic failure. However, the experiments show that v_{max}/v_{tot} does not increase monotonically, but instead experiences phases of delocalization of the fracture network away from the largest fracture (**Figure** 4). In some experiments, v_{max}/v_{tot} is smaller at the end of the experiment, immediately preceding failure, than at the beginning of the experiment (**Figure** 6). Only one experiment (granite #4) experiences a systematic increase in v_{max}/v_{tot} with only small perturbations. Thus, the fracture network in this experiment is dominated by one large fracture that grows and perhaps coalesces relatively faster than the other largest fractures. In general, however, the fracture networks are not dominated by the one largest fracture. The proportion of the experimental time (differential stress) in which the fracture networks experience localization toward the one largest fracture generally ranges from 40-70%, with two experiments hosting <20% (**Figure** 8).

In contrast, the experiments experience localization toward the largest set of fractures (with volumes >90th percentile) for a longer period of time than toward the one largest fracture, up to 80% of the applied differential stress (**Figure** 8). Tracking the proportion of the sum of the volumes >90th percentile to the total fracture volume, $\sum v_{90}/v_{tot}$, shows that all of the experiments host larger $\sum v_{90}/v_{tot}$ in the scan acquired immediately preceding failure than in the initial scan. Moreover, $\sum v_{90}/v_{tot}$ generally increases throughout each experiment, with only small episodes of delocalization (**Figure** 5). Thus, a more general description of fracture network development includes the growth and coalescence of several tens or hundreds of large fractures, rather than only one (e.g., **Figure** 12).

Using the localization metric that produces longest periods of increasing localization, the experiments tend to host localization for only up to 80% of the time (**Figure** 8). Thus, the fracture network does not continually localize toward the largest set of fractures, but also experiences phases with only minor changes in localization and short periods of delocalization. This evolution matches observations of low magnitude seismicity in southern and Baja California preceding several $M > 7$ earthquakes (*Ben-Zion & Zaliapin*, 2020).

The evolving fracture geometry and how it interacts with fractures and other heterogeneities likely triggers these episodes of delocalization. For example, a fracture may begin to grow and coalesce in one portion of the rock core, but then become impeded when it propagates into the stress shadow of another fracture or a mechanical heterogeneity. When this first

fracture arrests its growth, other large fractures may propagate and coalesce faster. Whether one fault propagates or not, and thus how fault networks develop, depend on the local tensile and shear stresses that develop at the fault tips (e.g., *Paterson & Wong*, 2005). These local stress concentrations influence the global mechanical efficiency of the system, suggesting that the efficiency of a system can predict whether a fault will propagate, and fault network development in general (e.g., *Cooke & Madden*, 2014). Numerical models suggest that fracture propagation will only occur when the energetic cost of propagation is lower than the gain in efficiency produced by that propagation (*Del Castello & Cooke*, 2007). Following this energy budget formulation, fracture propagation and subsequent slip can reduce the total internal work expended in diffuse host rock deformation while increasing the frictional work done against slip (e.g., *Madden et al*., 2017; *McBeck et al*., 2018, 2019). Thus, faults may propagate and slip only when the efficiency gained by reducing off-fault deformation (the decrease in internal work) is greater than the energy consumed in fracture growth and slip (the increase in frictional work and work of fault propagation).

The precise geometry of a fracture network, and whether it is dominated by one large fracture or several large fractures, has significant implications for fluid flow in the network, and the relationship between porosity and permeability. If the porosity of a rock volume arises from one dominant fracture, then the resulting permeability may be at the higher end of estimates. Instead, if the porosity arises from several large unconnected fractures, then the permeability may be lower than expected. The evolving and varying dominance of the largest fracture in these experiments underscore the importance of fluid flow simulations and experimental measurements when constraining permeability (e.g., *Dardis & McCloskey*, 1998; *Bernab*é *et al*., 2003; *Costa,* 2006; *Watanabe et al.*, 2009; *Zhao et al*., 2021).

4.2 Fracture network planarity

Tracking the similarity of the largest set of fractures to a plane with the r^2 score indicates that this set of fractures does not systematically localize toward the final failure plane throughout the experiment. Instead, each experiment hosts short phases of delocalization in which the r^2 score temporarily decreases or remains at similar values (**Figure** 9). If fracture networks develop from one dominant fracture that continually grows at the expense of others (**Figure** 12), then the r^2 score may tend to increase monotonically. However, because one fracture does not tend to dominate the full fracture network throughout all of the experiments, the evolving geometry of the largest set of fractures does not systematically increase toward planarity.

The planarity immediately preceding failure of the largest set of fractures, with volumes >90^{th} percentile, differs in the experiments on granite and monzonite (**Figure** 10). The r^2 score is generally higher for the monzonite experiments than for the granite experiments. Similarly, the mean distance of the largest fractures to the failure plane is generally smaller for the monzonite experiments than for the granite experiments. Thus, the fracture network that develops immediately preceding failure in the monzonite experiments more closely matches a plane than the network that develops in the granite experiments. This difference may arise from the higher confining stress applied to the monzonite experiments (25-35 MPa) compared to the granite experiments (5-10 MPa). The higher confining stress could promote greater localization of the fracture network to a plane in the monzonite experiments. Previous laboratory experiments demonstrate that higher confining stress can produce localized shear failure planes, while rocks under lower confinement fail via more distributed axial splitting (e.g., *Amann et al*., 2012). These laboratory results are also consistent with observations that

indicate that earthquake-induced rock damage in southern California is more localized and continuous at greater depth than near the surface (*Ben-Zion & Zaliapin*, 2019).

The larger mean grain size of the monzonite compared to the granite could also contribute to this difference in localization. Grain boundaries in crystalline rocks can influence where fractures nucleate because the constitutive minerals have varying stiffness (e.g., *Tapponnier & Brace,* 1976; *Moore & Lockner*, 1995). The material contrast produces differential compaction that leads to stress concentrations. The smaller grain size in the granite could lead to more sites of fracture nucleation and termination at the edges of minerals of different stiffnesses than the monzonite. The resulting greater number of sites of nucleation and termination could then produce more delocalized fracture networks in the granite than the monzonite.

In most experiments, the Gini coefficient and the mean distance to the failure plane are relatively constant, and then accelerate and decelerate close to macroscopic failure, respectively (**Figure** 11). The timing of this change in rate occurs near or slightly before the macroscopic yield point (within 10 MPa of differential stress) in some of the experiments (e.g., granite #2, monzonite #4 and #5), while in others this change occurs at least 20 MPa of differential stress before the yield point (e.g., granite #4). Thus, the reorganization of the fracture network that includes accelerating localization toward the largest set of fractures often precedes the macroscopic yield point. The acceleration of fracture network localization produces increasingly larger changes in the axial contraction for equal increments of differential stress. Fracture network localization may coincide in time with a transition from slower to faster fracture growth (e.g., *Thompson et al*., 2006). Because we load the rock core with differential stress steps, and stop increasing the differential stress to acquire a tomogram, the fracture growth that we capture in the tomograms is stable, and does not occur with an accelerating, unstable rate. Thus, in our experiments, the acceleration of fracture network localization may coincide in time with the transition from slower to faster fracture growth. Under more continuous differential stress or axial strain loading conditions, the localization of the fracture network may coincide with the transition from stable to unstable fracture growth. Previous work has also inferred a link between unstable fracture growth and fracture coalescence (e.g., *Nicksiar & Martin*, 2012). Other work has linked the transition from quasi-static to unstable fracture growth to a critical crack length (e.g., *Ohnaka & Kuwahara*, 1990).

5 Conclusions

We quantify the spatial distribution of fracture networks throughout six in situ X-ray tomography triaxial compression experiments approaching system-size failure under confining stress conditions of the upper crust. We assess the idea that one dominant fracture continually grows at the expense of others by tracking the ratio v_{max}/v_{tot} of the largest fracture volume relative to the total fracture volume throughout each experiment. The results show that v_{max}/v_{tot} does not systematically increase in the experiments. We then examine if a set of the largest fractures continually dominates deformation by tracking the sum of the volume of the fractures with volumes >90th percentile relative to the total fracture volume, $\sum v_{90}/v_{tot}$. This metric indicates that the fracture networks tend to increase in localization toward the largest set of fractures for up to 80% of the experimental time (differential stress). The evolution of this metric matches the evolution of the Gini coefficient. Experiments with higher applied confining stress tend to experience greater increases in localization.

Comparing the geometry of the set of the largest fractures to a plane with the r^2 score indicates that it is more similar to a plane in the monzonite experiments than the granite experiments. In addition, the mean distance between the plane and the set of fractures is smaller in the monzonite experiments than the granite experiments. The smaller mean grain size in the granite may produce more sites of fracture nucleation and termination, leading to more delocalized fracture networks that deviate further from a plane. The higher applied confining stress of the monzonite experiments (25-35 MPa) relative to the granite experiments (5-10 MPa) may also contribute to the more localized fracture networks in the monzonite experiments. Tracking these metrics of localization reveals a close association between the macroscopic yielding of the rock and the acceleration of the localization of the fracture network. Near yielding, $\sum v_{90}/v_{tot}$ and the Gini coefficient increase while the mean distance between the largest set of fractures and the final failure plane decreases. Macroscopic yielding occurs when the rate of fracture network localization increases. The macroscopic yielding may occur when the fractures begin to grow and coalesce faster, producing increasingly localized fracture networks.

Acknowledgements

We thank Elodie Boller, Paul Tafforeau, and Alexander Rack for advice about the design of the tomography setup, Benoît Cordonnier for the help with experiments, and Sanchez Technology for building the deformation apparatus. The Research Council of Norway (grant 300435 to JAM) and U.S. Department of Energy (award DE-SC0016520 to YBZ) funded this work. Sigma2-NIRD provided data storage (grant NS9073K). Beamtime was allocated at the European Synchrotron Radiation Facility (Long Term Proposal ES-295). The experimental data of time series of X-ray tomograms are available on Norstore: including the three monzonite samples (Renard, 2017, 2018), and the three Westerly granite samples (Renard, 2021).

References

Aben, F. M., Brantut, N., Mitchell, T. M., & David, E. C. (2019). Rupture energetics in crustal rock from laboratory-scale seismic tomography. Geophysical Research Letters, 46(13), 7337-7344.

Aben, F. M., Doan, M. L., Mitchell, T. M., Toussaint, R., Reuschlé, T., Fondriest, M., ... & Renard, F. (2016). Dynamic fracturing by successive coseismic loadings leads to pulverization in active fault zones. Journal of Geophysical Research: Solid Earth, 121(4), 2338-2360.

Amann, F., Kaiser, P., & Button, E. A. (2012). Experimental study of brittle behavior of clay shale in rapid triaxial compression. Rock Mechanics and Rock Engineering, 45(1), 21-33.

Buades, A., Coll, B., & Morel, J. M. (2005, June). A non-local algorithm for image denoising. In 2005 IEEE Computer Society Conference on Computer Vision and Pattern Recognition (CVPR'05) (Vol. 2, pp. 60-65). IEEE.

Ben-Zion, Y., & Sammis, C. G. (2003). Characterization of fault zones. Pure and applied geophysics, 160(3), 677-715.

Ben-Zion, Y., & Zaliapin, I. (2019). Spatial variations of rock damage production by earthquakes in southern California. Earth and Planetary Science Letters, 512, 184-193.

Ben-Zion, Y., & Zaliapin, I. (2020). Localization and coalescence of seismicity before large earthquakes. Geophysical Journal International, 223(1), 561-583.

533 Bergbauer, S., & Martel, S. J. (1999). Formation of joints in cooling plutons. Journal of
534 Structural Geology, 21(7), 821-835

535 Bernabé, Y., Mok, U., & Evans, B. (2003). Permeability-porosity relationships in rocks
536 subjected to various evolution processes. Pure and Applied Geophysics, 160(5), 937-960.

537 Brace, W. F., Paulding Jr, B. W., & Scholz, C. H. (1966). Dilatancy in the fracture of
538 crystalline rocks. Journal of Geophysical Research, 71(16), 3939-3953.

539 Chen, G., & Spetzler, H. (1993). Complexities of rock fracture and rock friction from
540 deformation of Westerly granite. pure and applied geophysics, 140(1), 95-121.

541 Cooke, M. L., & Madden, E. H. (2014). Is the Earth lazy? A review of work minimization in
542 fault evolution. Journal of Structural Geology, 66, 334-346.

543 Costa, A. (2006). Permeability-porosity relationship: A reexamination of the Kozeny-Carman
544 equation based on a fractal pore-space geometry assumption. Geophysical research
545 letters, 33(2).

546 Crider, J. G. (2015). The initiation of brittle faults in crystalline rock. Journal of Structural
547 Geology, 77, 159-174.

548 Dardis, O., & McCloskey, J. (1998). Permeability porosity relationships from numerical
549 simulations of fluid flow. Geophysical Research Letters, 25(9), 1471-1474.

550 Del Castello, M., & Cooke, M. L. (2007). Underthrusting-accretion cycle: Work budget as
551 revealed by the boundary element method. Journal of Geophysical Research: Solid
552 Earth, 112(B12).

553 Gini, C. (1921). Measurement of inequality of incomes. The economic journal, 31(121), 124-
554 126.

555 Goebel, T. H., Kwiatek, G., Becker, T. W., Brodsky, E. E., & Dresen, G. (2017). What
556 allows seismic events to grow big?: Insights from b-value and fault roughness analysis in
557 laboratory stick-slip experiments. Geology, 45(9), 815-818.

558 Griffith, A. A. (1921). VI. The phenomena of rupture and flow in solids. Philosophical
559 transactions of the royal society of london. Series A, containing papers of a mathematical or
560 physical character, 221(582-593), 163-198.

561 De Joussineau, G., Mutlu, O., Aydin, A., & Pollard, D. D. (2007). Characterization of strike-
562 slip fault–splay relationships in sandstone. Journal of Structural Geology, 29(11), 1831-1842.

563 Kandula, N., Cordonnier, B., Boller, E., Weiss, J., Dysthe, D. K., & Renard, F. (2019).
564 Dynamics of microscale precursors during brittle compressive failure in Carrara
565 marble. Journal of Geophysical Research: Solid Earth, 124(6), 6121-6139.

566 Kattenhorn, S. A., & Marshall, S. T. (2006). Fault-induced perturbed stress fields and
567 associated tensile and compressive deformation at fault tips in the ice shell of Europa:
568 implications for fault mechanics. Journal of structural geology, 28(12), 2204-2221.

569 Kemeny, J. M., & Cook, N. G. (1991). Micromechanics of deformation in rocks.
570 In Toughening mechanisms in quasi-brittle materials (pp. 155-188). Springer, Dordrecht.

571 Kranz, R. L. (1983). Microcracks in rocks: a review. Tectonophysics, 100(1-3), 449-480.

572 Horii, H., & Nemat-Nasser, S. (1986). Brittle failure in compression: splitting faulting and
573 brittle-ductile transition. Philosophical Transactions of the Royal Society of London. Series
574 A, Mathematical and Physical Sciences, 319(1549), 337-374.

575 Lei, X., Kusunose, K., Rao, M. V. M. S., Nishizawa, O., & Satoh, T. (2000). Quasi-static
576 fault growth and cracking in homogeneous brittle rock under triaxial compression using
577 acoustic emission monitoring. Journal of Geophysical Research: Solid Earth, 105(B3), 6127-
578 6139.

579 Lyakhovsky, V., Hamiel, Y., & Ben-Zion, Y. (2011). A non-local visco-elastic damage
580 model and dynamic fracturing. Journal of the Mechanics and Physics of Solids, 59(9), 1752-
581 1776.

582 Isida, M. (1971). Effect of width and length on stress intensity factors of internally cracked
583 plates under various boundary conditions. International Journal of Fracture Mechanics, 7(3),
584 301-316.

585 Madden, E. H., Cooke, M. L., & McBeck, J. (2017). Energy budget and propagation of faults
586 via shearing and opening using work optimization. Journal of Geophysical Research: Solid
587 Earth, 122(8), 6757-6772.

588 McBeck, J. A., Aiken, J. M., Mathiesen, J., Ben-Zion, Y., & Renard, F. (2020a). Deformation
589 precursors to catastrophic failure in rocks. Geophysical Research Letters, 47(24),
590 e2020GL090255.

591 McBeck, J., Aiken, J. M., Ben-Zion, Y., & Renard, F. (2020b). Predicting the proximity to
592 macroscopic failure using local strain populations from dynamic in situ X-ray tomography
593 triaxial compression experiments on rocks. Earth and Planetary Science Letters, 543, 116344.

594 McBeck, J., Cooke, M., Souloumiac, P., Maillot, B., & Mary, B. (2018). The influence of
595 detachment strength on the evolving deformational energy budget of physical accretionary
596 prisms. Solid Earth, 9(6), 1421-1436

597 McBeck, J., Cordonnier, B., Mair, K., & Renard, F. (2019). The evolving energy budget of
598 experimental faults within continental crust: Insights from in situ dynamic X-ray
599 microtomography. Journal of Structural Geology, 123, 42-53.

600 McBeck, J. A., Zhu, W., & Renard, F. (2021). The competition between fracture nucleation,
601 propagation, and coalescence in dry and water-saturated crystalline rock. Solid Earth, 12(2),
602 375-387.

603 Miao, S., Pan, P. Z., Zhao, X., Shao, C., & Yu, P. (2021). Experimental study on damage and
604 fracture characteristics of Beishan granite subjected to high-temperature treatment with DIC
605 and AE techniques. Rock Mechanics and Rock Engineering, 54(2), 721-743.

606 Moir, H., Lunn, R. J., Shipton, Z. K., & Kirkpatrick, J. D. (2010). Simulating brittle fault
607 evolution from networks of pre-existing joints within crystalline rock. Journal of Structural
608 Geology, 32(11), 1742-1753.

609 Moore, D. E., & Lockner, D. A. (1995). The role of microcracking in shear-fracture
610 propagation in granite. Journal of Structural Geology, 17(1), 95-114

611 Paterson, M. S., & Wong, T. F. (2005). Experimental rock deformation-the brittle field.
612 Springer Science & Business Media.

613 Peng, S., & Johnson, A. M. (1972, January). Crack growth and faulting in cylindrical
614 specimens of Chelmsford granite. In International Journal of Rock Mechanics and Mining
615 Sciences & Geomechanics Abstracts (Vol. 9, No. 1, pp. 37-86). Pergamon.

616 Rawling, G. C., Baud, P., & Wong, T. F. (2002). Dilatancy, brittle strength, and anisotropy of
617 foliated rocks: Experimental deformation and micromechanical modeling. Journal of
618 Geophysical Research: Solid Earth, 107(B10), ETG-8

619 Renard, F. (2017). Critical evolution of damage towards system size failure in a crystalline
620 rock [Data set]. Norstore. doi:10.11582/2017.00025.

621 Renard, F. (2018). Volumetric and shear processes in crystalline rock during the approach to
622 faulting [Data set]. Norstore. doi:10.11582/2018.00023.

623 Renard, F. (2021). X-ray tomography data of Westerley granite [Data set]. Norstore.
624 doi:10.11582/2021.00002.

625 Renard, F., Cordonnier, B., Dysthe, D. K., Boller, E., Tafforeau, P., & Rack, A. (2016). A
626 deformation rig for synchrotron microtomography studies of geomaterials under conditions
627 down to 10 km depth in the Earth. Journal of Synchrotron Radiation, 23(4), 1030-1034.

628 Renard, F., McBeck, J., Cordonnier, B., Zheng, X., Kandula, N., Sanchez, J. R., & Dysthe, D.
629 K. (2019a). Dynamic in situ three-dimensional imaging and digital volume correlation
630 analysis to quantify strain localization and fracture coalescence in sandstone. Pure and
631 Applied Geophysics, 176(3), 1083-1115.

632 Renard, F., McBeck, J., Kandula, N., Cordonnier, B., Meakin, P., & Ben-Zion, Y. (2019b).
633 Volumetric and shear processes in crystalline rock approaching faulting. Proceedings of the
634 National Academy of Sciences, 116(33), 16234-16239.

635 Renard, F., Cordonnier, B., Kobchenko, M., Kandula, N., Weiss, J., & Zhu, W. (2017).
636 Microscale characterization of rupture nucleation unravels precursors to faulting in
637 rocks. Earth and Planetary Science Letters, 476, 69-78.

638 Renard, F., Weiss, J., Mathiesen, J., Ben Zion, Y., Kandula, N., Cordonnier, B. (2018)
639 Critical evolution of damage towards system-size failure in crystalline rock, Journal of
640 Geophysical Research, 123, 1969-1986.

641 Sammis, C. G., & Ashby, M. F. (1986). The failure of brittle porous solids under compressive
642 stress states. Acta Metallurgica, 34(3), 511-526.

643 Segall, P., & Pollard, D. D. (1983). Nucleation and growth of strike slip faults in
644 granite. Journal of Geophysical Research: Solid Earth, 88(B1), 555-568.

645 Schubnel, A., Nishizawa, O., Masuda, K., Lei, X. J., Xue, Z., & Guéguen, Y. (2003).
646 Velocity measurements and crack density determination during wet triaxial experiments on
647 Oshima and Toki granites. In Thermo-Hydro-Mechanical Coupling in Fractured Rock (pp.
648 869-887). Birkhäuser, Basel.

649 Tapponnier, P., & Brace, W.F. (1976). Development of stress-induced microcracks in
650 Westerly granite. International Journal of Rock Mechanics and Mining Sciences &
651 Geomechanics Abstracts, 13(4), 103-112. Pergamon.

652 Thompson, B. D., Young, R. P., & Lockner, D. A. (2006). Fracture in Westerly granite under
653 AE feedback and constant strain rate loading: nucleation, quasi-static propagation, and the
654 transition to unstable fracture propagation. Pure and Applied Geophysics, 163(5), 995-1019.

655 Watanabe, N., Hirano, N., & Tsuchiya, N. (2009). Diversity of channeling flow in
656 heterogeneous aperture distribution inferred from integrated experimental-numerical analysis
657 on flow through shear fracture in granite. Journal of Geophysical Research: Solid
658 Earth, 114(B4), B04208.

659 Wong, T. F. (1982). Micromechanics of faulting in Westerly granite. In International Journal
660 of Rock Mechanics and Mining Sciences & geomechanics abstracts (Vol. 19, No. 2, pp. 49-
661 64). Pergamon.

662 Wu, X. Y., Baud, P., & Wong, T. F. (2000). Micromechanics of compressive failure and
663 spatial evolution of anisotropic damage in Darley Dale sandstone. International Journal of
664 Rock Mechanics and Mining Sciences, 37(1-2), 143-160.

665 Zabler, S., Rack, A., Manke, I., Thermann, K., Tiedemann, J., Harthill, N., & Riesemeier, H.
666 (2008). High-resolution tomography of cracks, voids and micro-structure in greywacke and
667 limestone. Journal of Structural Geology, 30(7), 876-887.

668 Zhao, C., Zhou, Y., Zhao, C., & Bao, C. (2018). Cracking processes and coalescence modes
669 in rock-like specimens with two parallel pre-existing cracks. Rock Mechanics and Rock
670 Engineering, 51(11), 3377-3393.

671 Zhao, Z., Zhao, Y., Jiang, Z., Guo, J., and Zhang, R. (2021). Investigation of Fracture
672 Intersection Behaviors in Three-Dimensional Space Based on CT Scanning Experiments.
673 Rock Mech Rock Eng. https://doi.org/10.1007/s00603-021-02587-9.

Figures

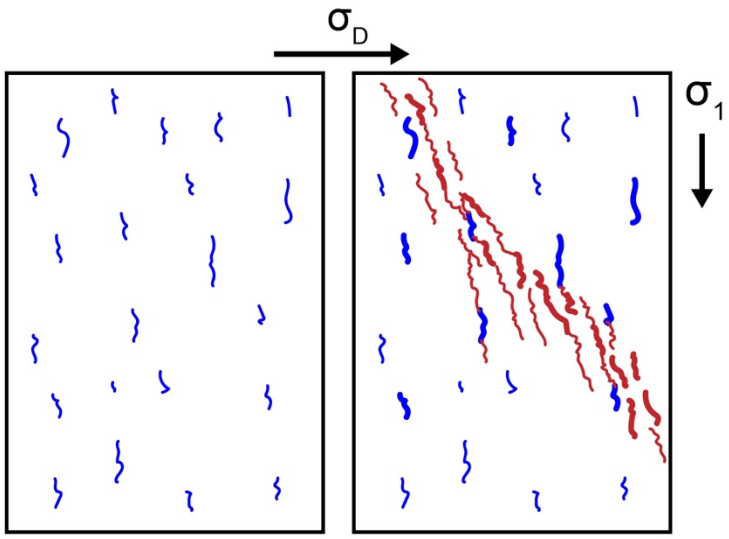

Figure 1. Transition from stable (left) to unstable (right) fracture network development via coalescence of fractures with increasing differential stress, σ_D. Left: Under lower σ_D, microfractures nucleate and grow parallel to the main compressive stress, σ_1. Right: With increasing σ_D, approaching system-size failure, the microfractures grow, interact, and link to form a connected fault.

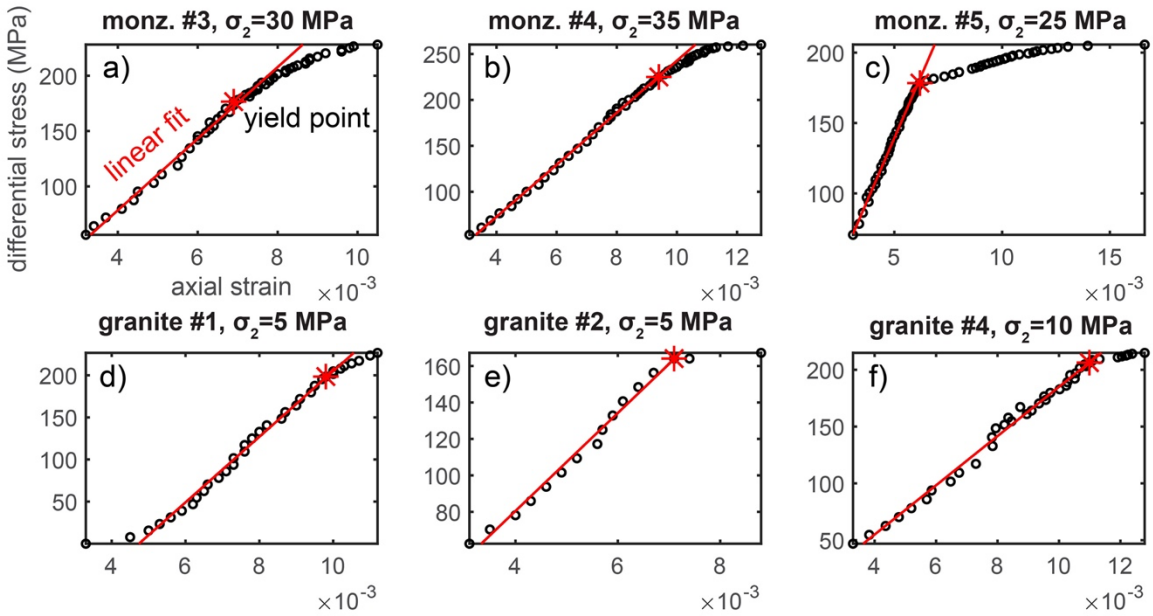

Figure 2. Differential stress versus axial strain relationships for the six examined experiments: a) monzonite #3, b) monzonite #4, c) monzonite #5, d) granite #1, e) granite #2, and f) granite #4. Black circles show the conditions when an X-ray tomogram was acquired. Red lines show the linear fit of the early portion of the data. Red stars show the identified yield point, when the data diverges from the linear fit. The title of each plot shows the experiment abbreviation (**Table** 1), and applied confining stress, σ_2. In experiment monz. #4, we applied a pore fluid pressure, p=5 MPa.

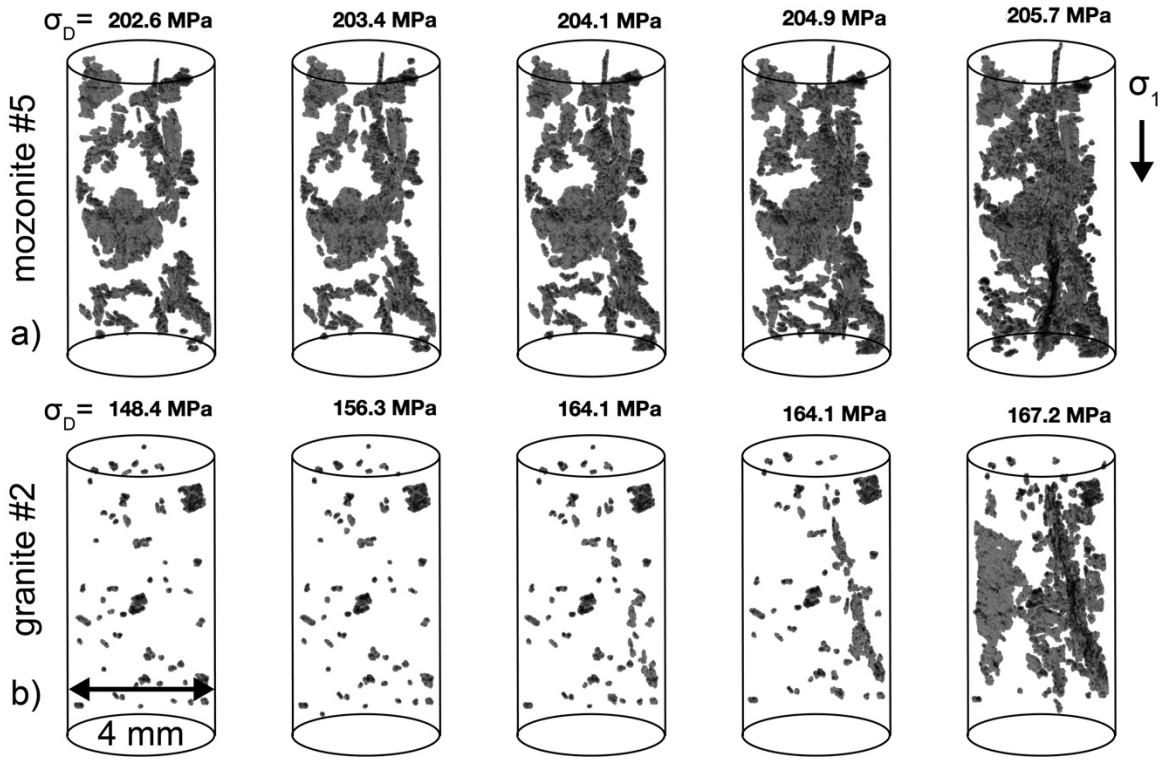

Figure 3. Fracture network development in the final five tomograms preceding macroscopic failure in experiment monzonite #5 (a) and granite #2 (b). Black regions show the fractures with volumes greater than the 90th percentile of the population. Numbers at the top of the cores show the differential stress applied on the sample when the scan was acquired.

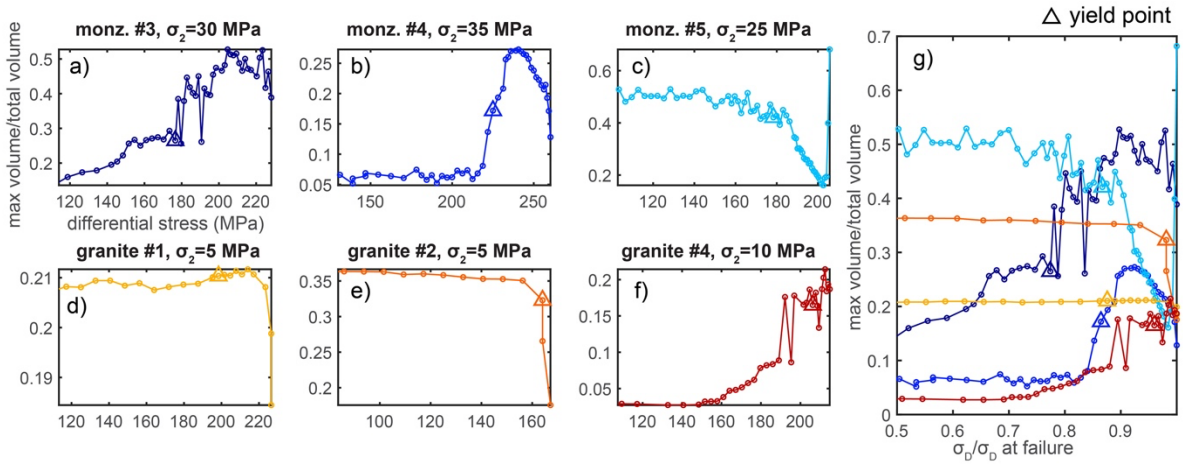

Figure 4. Evolution of the maximum fracture volume divided by the total volume of fractures, v_{max}/v_{tot}, throughout each individual experiment (a-f), and for all the experiments (g). Color of the lines in (g) matches the colors of each experiment shown in (a-f). Triangles show the conditions of the yield point. Increasing v_{max}/v_{tot} indicates that the fracture network is localizing toward the one largest fracture.

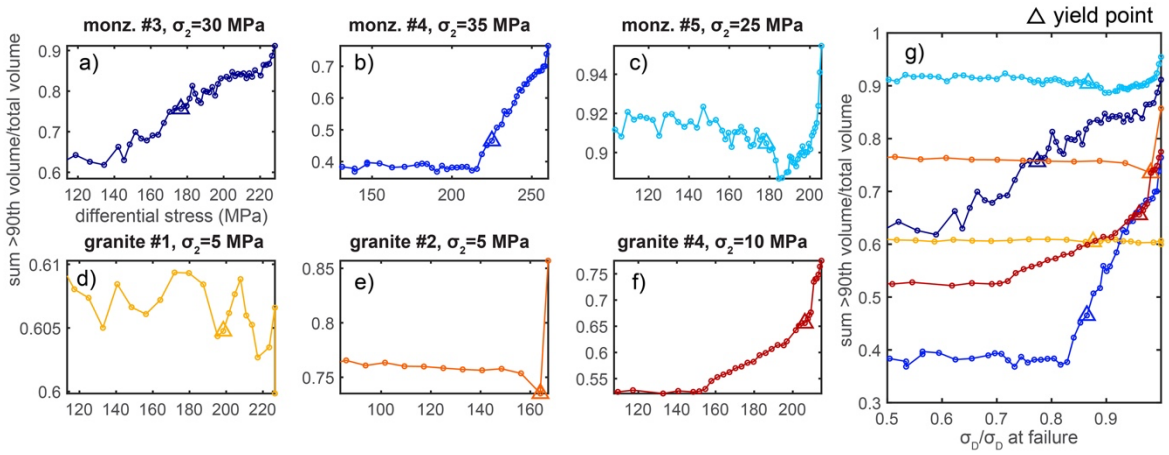

Figure 5. Evolution of the sum of the fracture volumes with values >90th percentile divided by the total volume of fractures, $\sum v_{90}/v_{tot}$, throughout each individual experiment (a-f), and for all the experiments (g). Color of the lines in (g) matches the colors of each experiment shown in (a-f). Triangles show the conditions of the yield point. Increasing $\sum v_{90}/v_{tot}$ indicates increasing localization toward the largest fractures in the network, with volumes >90th percentile.

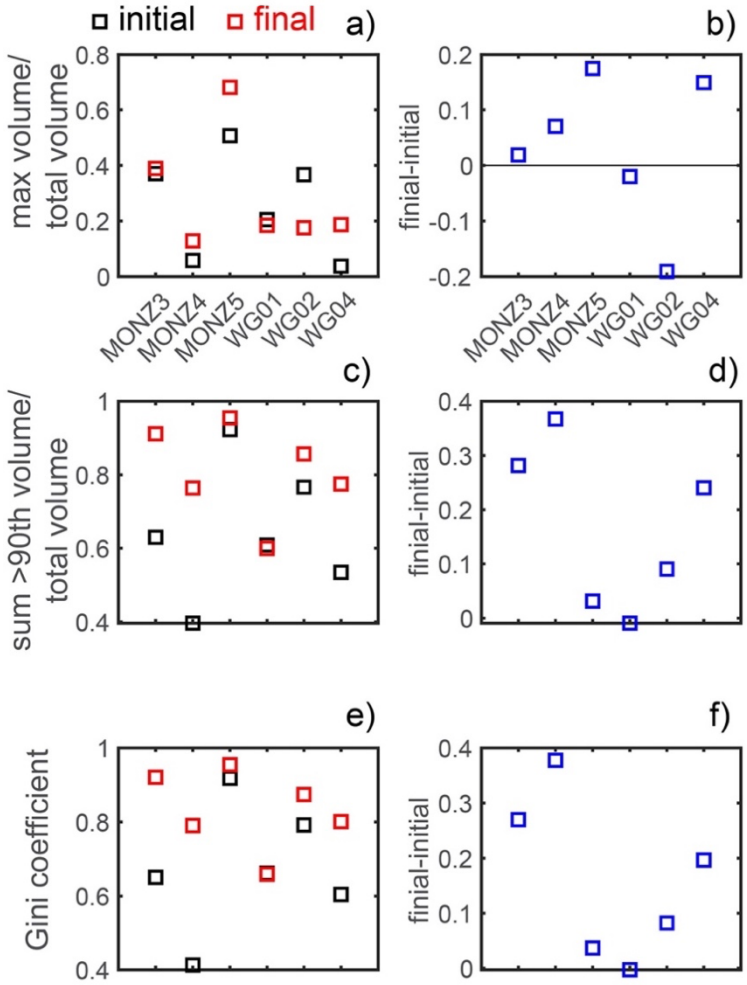

Figure 6. Difference in the v_{max}/v_{tot} (a-b), $\sum v_{90}/v_{tot}$ (c-d), and the Gini coefficient (e-f) from the initial and final tomogram acquired in each experiment. Positive changes from the initial

709 to final scan indicate increasing localization. The results of the Gini coefficient and
710 $\sum v_{90}/v_{tot}$ are nearly identical.

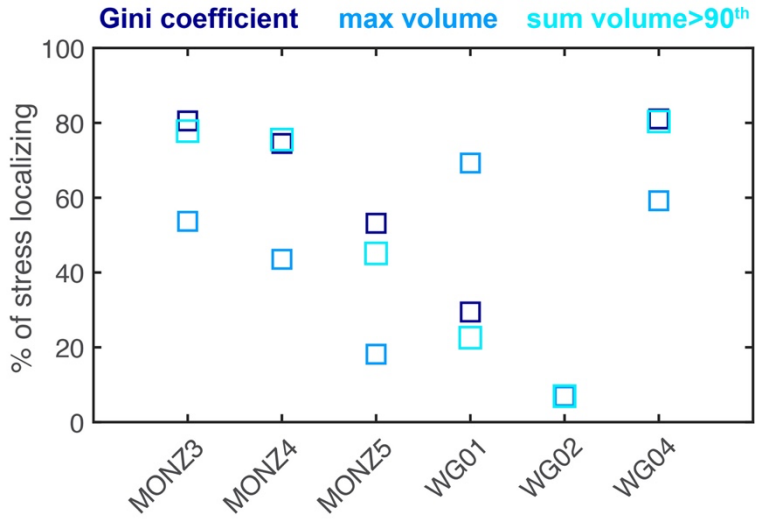

711

712 **Figure 7**. Percentage of the applied differential stress in which the Gini coefficient, v_{max}/v_{tot},
713 and $\sum v_{90}/v_{tot}$ show localization, i.e., increase from one scan to the next.

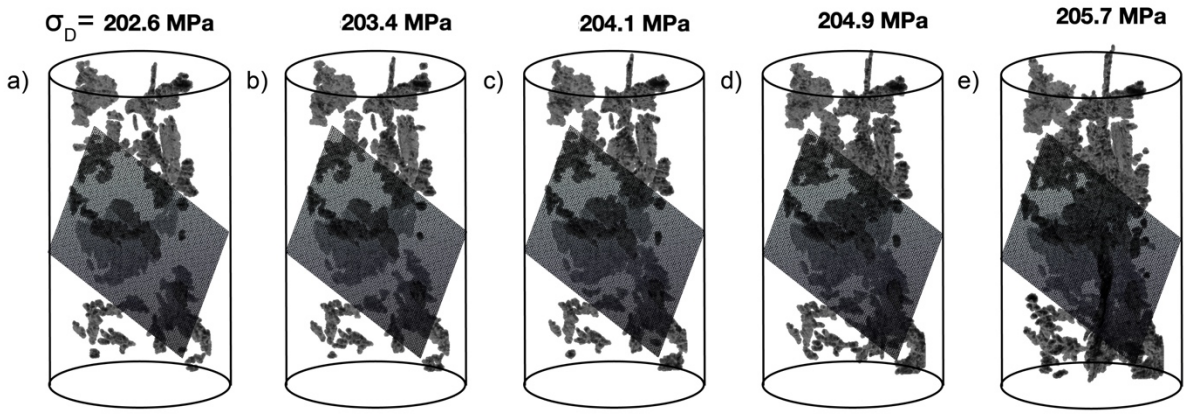

714

715 **Figure 8**. Largest fractures, with volumes >90th percentile, in the five scans acquired before
716 failure in the monzonite #5 experiment, and best fit plane of the final fault geometry. The
717 final failure plane is built from the scan acquired immediately preceding failure. Numbers at
718 the top of the cores show the differential stress when the scan was acquired.

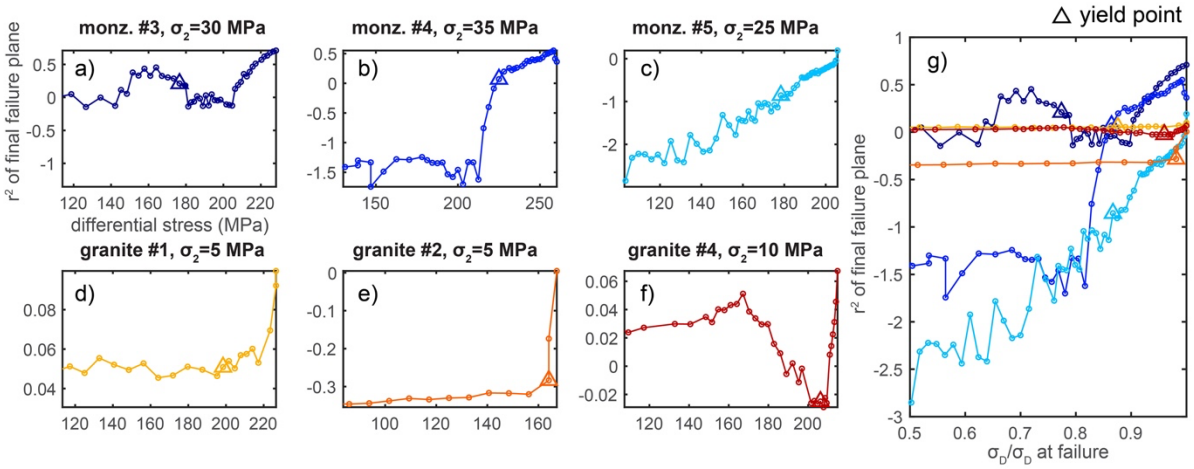

Figure 9. Evolution of the r^2 of the largest fractures and the final failure plane throughout each individual experiment (a-f), and for all the experiments (g). Color of the lines in (g) matches the colors of each experiment shown in (a-f). Triangles show the conditions of the yield point.

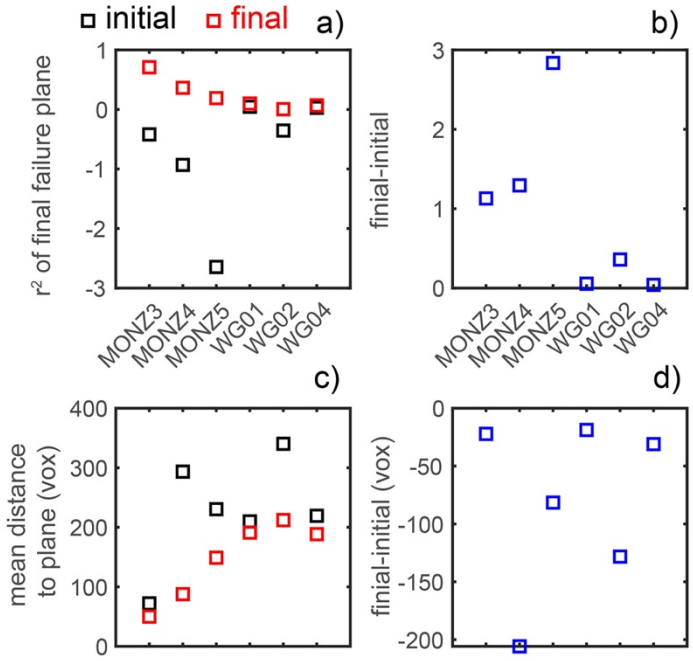

Figure 10. Difference in the r^2 score (a-b), and mean distance between the 10% largest fractures and the failure plane (c-d) from the initial and final tomogram acquired in each experiment. Positive and negative changes from the initial to final scan indicate increasing localization for the r^2 score and mean distance, respectively.

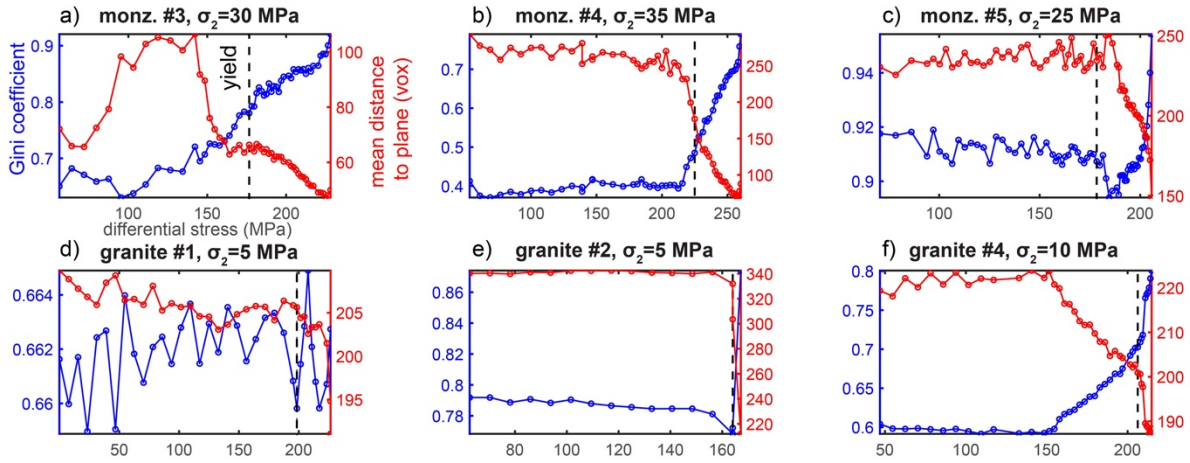

728
729 **Figure 11**. Evolution of the Gini coefficient and mean distance to the final failure plane in
730 each experiment. Increasing Gini coefficient indicates increasing localization, while
731 decreasing distance indicates increasing localization. Vertical black dashed lines indicate the
732 macroscopic yield point.

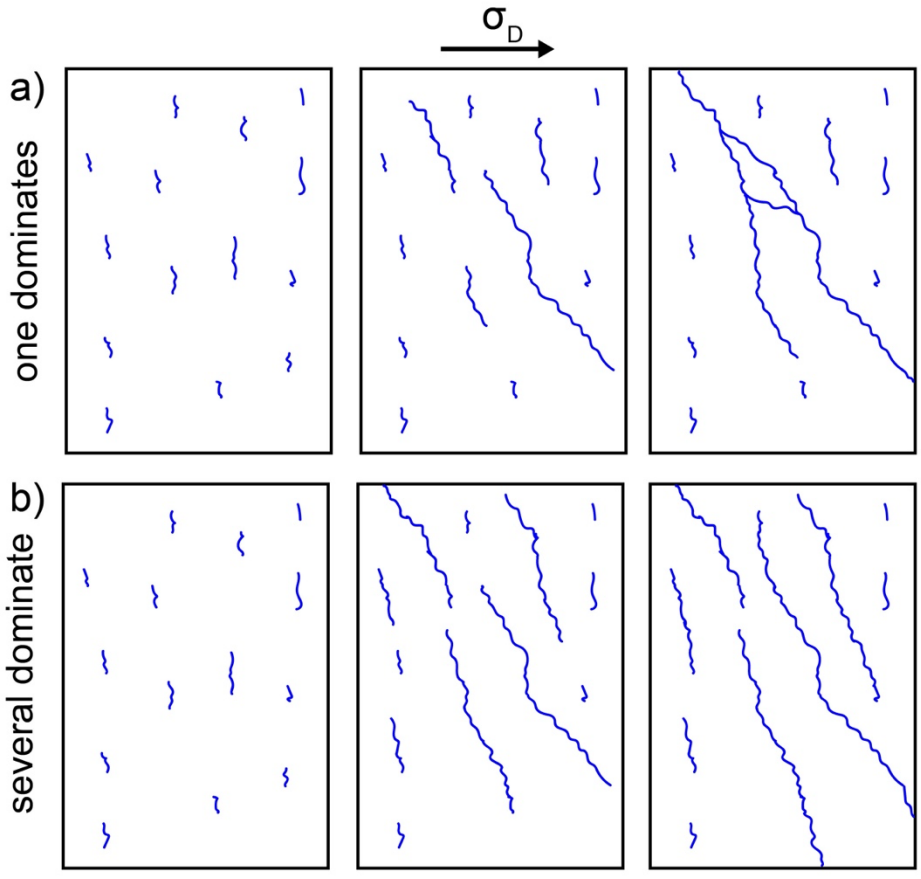

733

734 **Figure 12**. Fracture network development in a rock in which the one largest fracture
735 dominates development (a) and in which several of the largest fractures dominate (b). The
736 localization observed in experiments monzonite #3 and granite #4 most closely match (a),
737 while the other experiments most closely match (b) (e.g., **Figure** 4).

738

Experiment	Confining stress (MPa)	Pore pressure (MPa)
Monzonite #3	30	0
Monzonite #4	35	5
Monzonite #5	25	0
Granite #1	5	0
Granite #2	5	0
Granite #4	10	0

739

740 **Table 1**. Conditions of each experiment.